

# Micro Power Generator for Harvesting Low-Frequency and Nonperiodic Vibrations

Tzeno Galchev, *Member, IEEE*, Hanseup Kim, *Member, IEEE*, and Khalil Najafi, *Fellow, IEEE*

**Abstract**—This paper presents a new inertial power generator for scavenging low-frequency nonperiodic vibrations called the Parametric Frequency-Increased Generator (PFIG). The PFIG utilizes three magnetically coupled mechanical structures to initiate high-frequency mechanical oscillations in an electromechanical transducer. The fixed internal displacement and dynamics of the PFIG allow it to operate more effectively than resonant generators when the ambient vibration amplitude is higher than the internal displacement limit of the device. The design, fabrication, and testing of an electromagnetic PFIG are discussed. The developed PFIG can generate a peak power of  $163 \mu\text{W}$  and an average power of  $13.6 \mu\text{W}$  from an input acceleration of  $9.8 \text{ m/s}^2$  at 10 Hz, and it can operate at frequencies up to 65 Hz, giving it an unprecedented operating bandwidth and versatility. The internal volume of the generator is  $2.12 \text{ cm}^3$  ( $3.75 \text{ cm}^3$  including the casing). The harvester has a volume figure of merit of 0.068% and a bandwidth figure of merit of 0.375%. These values, although seemingly low, are the highest reported in the literature for a device of this size and operating in the difficult frequency range of  $\leq 20 \text{ Hz}$ . [2011-0023]

**Index Terms**—Energy harvesting, energy scavenging, Frequency-Increased Generator (FIG), frequency up-conversion, low frequency, Parametric Frequency-Increased Generator (PFIG), parametric generator, vibration harvesting.

## I. INTRODUCTION

**D**RAMATIC advancements in electronics continue to bolster the vision of a world full of wireless sensor networks, “smart” automation systems, and ambient intelligence. One of the greatest hurdles to realizing this vision is the availability of cheap long-lasting energy. While wired power sources remain an option, they limit the utility and increase the cost of wireless electronics. Wireless power supplies are the only viable option for these systems because they complement their portability and reduce installation costs. Stored capacity (batteries) [1] or generative (fuel cell and combustible fuel) [2], [3] energy sources can be employed to extend the range of wireless sensors and to lower overhead. However, these technologies introduce a significant maintenance cost for replacement and recharging, which often exceeds the cost of wired power [4]. Renewable

sources of energy, or energy harvesting, have gained significant momentum over the past decade, because technological advances in wireless electronics have reduced power consumption and opened the door for powering wireless sensors, implantable devices, and other wireless gadgets using harvested ambient energy. Eliminating maintenance and battery replacement enables many long-lifetime applications both technologically and from a standpoint of cost.

A number of energy harvesting approaches have been examined as potential sources of renewable power. Examples are solar power [5], temperature gradients [6], pressure differentials [7], and flow of liquids and gases [8]. However, one of the most abundant energy sources is ambient motion [9]–[11]. Vibrations have garnered the most interest because of their abundance, high theoretically achievable conversion efficiency, and transmissibility through different media. Over the past decade, a great deal of research has gone into developing vibration harvesters based on electromagnetic, piezoelectric, and electrostatic transduction [12]. A vast majority of these efforts use second-order spring–mass–damper resonant systems, where the resonant frequency of the generator is matched to the vibrations present in the intended application environment. Resonant generators capable of harvesting linear vibrations were introduced by Shearwood *et al.* [13], [14]. The authors described the initial design methodology for inertial micro-generators and they microfabricated the first electromagnetic generator. Roundy *et al.* presented one of the most efficient piezoelectric harvesters to date in their seminal work that used a piezoelectric bimorph cantilever [9]. Variations on this theme have been published by many authors since. An initial design methodology for electrostatic harvesters was developed by Meninger *et al.* [15], [16].

The vibration harvesting efforts cited earlier as well as many that followed only apply to one specific type of vibration, mainly produced by “man-made” sources such as motors or other machinery. These vibrations are periodic and typically have a frequency  $\geq 60 \text{ Hz}$ . Work in the frequency range below 60 Hz is scarce [12], with maximum harvester effectiveness [10] and volume figure of merit [10] values  $< 0.1\%$  in the  $< 40 \text{ Hz}$  frequency range. However, it is at these low frequencies that available vibration energy can be found in many practical applications including environmental monitoring, agricultural automation, structural monitoring, security and military applications, and medical and body-worn devices. Additionally, some of the vibrations in these applications, particularly those in the very low end of the frequency spectrum, do not provide power at a single fundamental frequency, and hence, the concept of bandwidth becomes extremely important.

Manuscript received January 24, 2011; revised April 7, 2011; accepted May 25, 2011. Date of publication July 27, 2011; date of current version August 3, 2011. This work was supported by the Engineering Research Centers Program of the National Science Foundation under Award EEC-9986866. Subject Editor R. Ghodssi.

The authors are with the Engineering Research Center for Wireless Integrated MicroSystems (WIMS), University of Michigan, Ann Arbor, MI 48109-2122 USA (e-mail: tgalchev@umich.edu; hanseup@gmail.com; najafi@umich.edu).

Color versions of one or more of the figures in this paper are available online at <http://ieeexplore.ieee.org>.

Digital Object Identifier 10.1109/JMEMS.2011.2160045

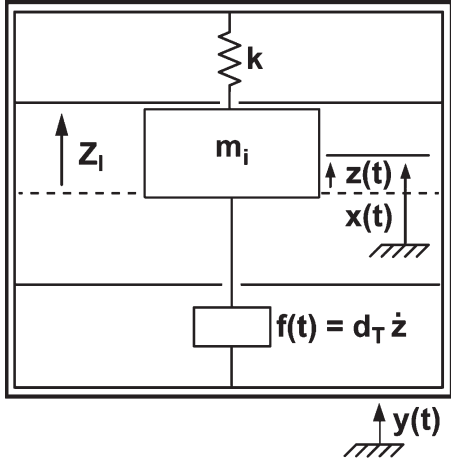


Fig. 1. Generic model of an inertial micro power generator.

This paper discusses the modeling and analysis of a new vibration generator architecture designed for harvesting low-frequency ambient vibrations. The Parametric FIG (PFIG) architecture was previously demonstrated using a bench-top prototype [17] and a self-contained version [18]. The detailed design, fabrication, and test results from an optimized miniature electromagnetic PFIG generator, similar in overall structure and layout to that in [18], are presented in this paper. Following the introduction, a brief review of important concepts related to vibration harvesting and the challenges specific to harvesting low-frequency vibrations are given in Section II. The PFIG generator is presented in Section III, and a framework for analyzing PFIG generators is discussed. Section IV explores the design and fabrication of a miniature electromagnetic PFIG implementation. The testing methodology and results are shown in Section V. The results are put in context of the state-of-the-art in performance in Section VI, along with an examination of possible future work and improvements. The conclusions of the study are presented in Section VII.

## II. BASIC THEORY AND CHALLENGES IN LOW-FREQUENCY HARVESTING

It is an oft-encountered misconception that all vibration harvesters can simply be designed as resonant systems irrespective of the amplitude or frequency of the source motion. Reported efficiencies for generators harvesting low-frequency vibrations are orders of magnitude lower than those harvesting higher frequency vibrations [10], [12], [19]. A number of additional challenges need to be addressed when harvesting low-frequency vibrations.

### A. Resonant Vibration Harvesters

In order to discuss the challenges of scavenging low-frequency vibrations as well as the merits of the PFIG generator, it is necessary to review some of the basic theory behind vibration harvesters. A typical generator consists of a rigid casing with a seismic mass suspended inside, as shown in Fig. 1. The mass moves relative to the casing in response to an externally applied displacement. During this motion, it

performs work against a damping force  $f(t)$  opposing the movement of the mass, thereby generating energy. The displacement of the mass relative to the frame is denoted by  $z(t)$ . For simplicity, the source motion will be considered harmonic  $y(t) = Y_o \cos \omega t$ , with  $Y_o$  being the source motion amplitude. Lastly, the maximum displacement for a particular device will be referred to as  $Z_l$ . The differential equation of motion for a typical generator is shown in

$$m\ddot{z} + d_T \dot{z}(t) + kz(t) = -m\ddot{y}(t). \quad (1)$$

The equation is normalized using the damping factor  $\zeta = d_T/2m\omega_n$ , where  $\omega_n$  is the natural frequency  $\omega_n = \sqrt{k/m}$  and  $d_T$  is the damping constant. The energy dissipated in the damper every cycle, in other words, the converted energy, is given by integrating the damping force  $f = d_T \dot{z}$  over a full cycle

$$W_d = \oint f dz. \quad (2)$$

This analysis assumes viscous damping, which is often a good approximation for electromagnetic and piezoelectric generators. Based on the fundamental statements made in (1) and (2), the power that can be converted by the device in Fig. 1 is

$$P = \frac{\zeta \eta^3 Y_o^3 \omega^3 m}{[1 - \eta^2]^2 + [2\zeta \eta]^2} \quad (3)$$

where  $\eta = \omega/\omega_n$ . The derivation of (3), as well as a more thorough analysis pertaining to the basic theory of vibration harvesters, is out of the scope of this paper; interested readers are referred to the very comprehensive analysis by Mitcheson *et al.* [20].

Equation (3) predicts that the generated power can increase without bound at resonance ( $\eta = 1$ ). Mathematically, this happens because the source is assumed to have infinite power, no internal displacement limit is taken into account, and parasitic dissipative forces are not considered. A more realistic formulation for maximum power, taking into account an optimal damping ratio and a displacement limit, is given by [20]

$$P_{\max} = Y_o^2 \omega^3 m \frac{1}{2\eta} \left( \frac{Z_l}{Y_o} \right)^2 \sqrt{\eta^4 \left( \frac{Y_o}{Z_l} \right)^2 - (1 - \eta^2)^2}. \quad (4)$$

At resonance ( $\eta = 1$ ), (4) simplifies to

$$P_{\text{res}} = \frac{1}{2} \omega^3 m Y_o Z_l. \quad (5)$$

The analysis, so far, has assumed that there are no parasitic losses in the system. When the parasitic damping is comparable in scale to the electrical damping of the system, it must be included in the calculations. This means that the damping coefficient must be corrected to  $d_T = d_p + d_e$ , where  $d_p$  is the open-circuit parasitic mechanical damping and  $d_e$  is the electrical damping of the transduction mechanism. It follows

that  $\zeta_T = \zeta_p + \zeta_e$  and that the quality factor of the system, which, in total, is equal to  $Q_T = \omega_n m / d_T$ , will be given by

$$\frac{1}{Q_T} = \frac{1}{Q_p} + \frac{1}{Q_e}. \quad (6)$$

The last issue that must be addressed when dealing with energy harvesters is to present relevant metrics of performance that will allow an evenhanded comparison. A good metric will normalize with respect to the incoming energy so that a fair comparison can be made, because conversion efficiency is a strong function of frequency and amplitude. A very useful metric is proposed by Mitcheson *et al.* [10] and is called the volume figure of merit ( $F_o M_v$ ), which compares device performance as a function of overall size

$$F_o M_v = \frac{\text{Useful Power Output}}{\frac{1}{2} Y_o \rho_{\text{AU}} \text{Vol}^{\frac{4}{3}} \omega^3}. \quad (7)$$

Here, the mass  $m$  and maximum displacement range  $Z_l$  are substituted with parameters for an idealized device with cubic geometry having the same volume but with a proof mass made of gold (one of the densest materials used in micromachining) occupying half of this volume and space for displacement occupying the other half. A real device cannot reach 100% in practice because some space must be taken up by the frame, suspension, and transducer components. Lastly, in order to account for bandwidth, a further modification called the bandwidth figure of merit ( $F_o M_{\text{BW}}$ ) is proposed [10]

$$F_o M_{\text{BW}} = F_o M_v \times \frac{BW_{3 \text{ dB}}}{\omega} \quad (8)$$

which is simply the volume figure of merit multiplied by the fractional bandwidth (in [9], a 1-dB bandwidth divided by the center frequency is used).

### B. Displacement Challenge

For a given acceleration, the amplitude of the vibration  $Y_o$  is inversely proportional to the square of the frequency, i.e.,  $Y_o \sim 1/\omega^2$ . As shown in (4), the power that can be generated from vibrations is  $P \sim (Z_l/Y_o)$  under optimal damping conditions. This means that the internal displacement limit of the generator  $Z_l$  has to be at least as large as the vibration amplitude to achieve high power. Generators to date have all reported  $\zeta_T < 1$ , meaning that they are underdamped and they require  $Z_l$  to be significantly larger than  $Y_o$ . This is not a coincidence, since it is clear that having a quality factor  $Q > 1$  is also desirable for power generation when working at resonance. However, at low frequencies, even small Qs (1–10) present a big barrier to the scalability of resonant generators, particularly when their dimensions reach the microscale range where typical displacements are constrained to 1–100  $\mu\text{m}$ . In addition, the increased displacement range at low frequencies, resulting from the  $Y_o \sim 1/\omega^2$  relationship, is a direct impediment to higher efficiency as it means that a larger volume is needed and the denominator in (7) increases significantly. Therefore, we define “low-frequency vibration” (where resonant generators are not

effective) as being any vibration where  $Y_o > Z_l$ . Thus, whether a frequency is low or not is dependent on the generator’s size.

### C. Frequency Dependence of Electromechanical Coupling

As was mentioned in Section II-A, electromagnetic and piezoelectric conversions can be approximated by linearizing and modeling them as viscously damped systems or ones where the force opposing the motion of the mass is proportional to the velocity of the mass ( $f = d\dot{z}$ ). This means that this force  $f$  will reduce as  $1/\omega$ , therefore weakening the electromechanical coupling of the system at low frequency (provided that  $d$  stays constant).

### D. Typical Applications and the Bandwidth Challenge

The low-frequency vibrations found in various scavenging applications are typically created from natural and environmental sources, rather than being created by machinery or other man-made means. Many of these natural vibration sources rely on random or semirandom phenomena, and their energy is spread over a certain band, for example, transportation and car vibrations (< 20 Hz), human motion (< 10 Hz), guard rail on the street (< 50 Hz), etc. These data are found in [21], and a number of other studies have been published, characterizing the vibrations in various locations and providing more examples [22], [23].

Two general approaches to dealing with the issue of bandwidth have been proposed: 1) passive or active tuning [24]–[27] and 2) combining a number of resonators with closely spaced natural frequencies to effectively achieve a greater bandwidth [28]. These approaches unfortunately do not provide much value in these applications. Low-frequency scavengers are already big due to their large mass and displacement limit; therefore, they cannot be arrayed. Additionally, tuning does not provide value when the vibrations change and are not known *a priori*. In order to harvest vibrations that are not periodic, nonresonant, or parametric, devices are necessary. An example of such a technology for harvesting human motion is discussed in [29].

## III. PFIG

To address the challenges outlined in the previous sections, a novel nonresonant generator architecture is designed. The PFIG, shown in Fig. 2(a), is designed to accommodate the large amplitudes associated with low-frequency vibrations. Furthermore, it is able to operate over a wide band of frequencies, since it works in a nonresonant fashion. The Parametric Frequency-Increased Generator (PFIG) utilizes a large inertial mass to couple kinetic energy from the ambient into the generator structure and to pass a portion of this kinetic energy to one of two FIGs. The FIGs then convert this mechanical energy into electrical energy via electromagnetic induction. Two FIGs are placed on either side of the inertial mass, oriented to face each other. Attached to the bottom of the FIG spring is a NdFeB magnet for power generation. On top, a smaller magnet is used to generate a magnetic force in order to latch the FIG and the inertial mass together.

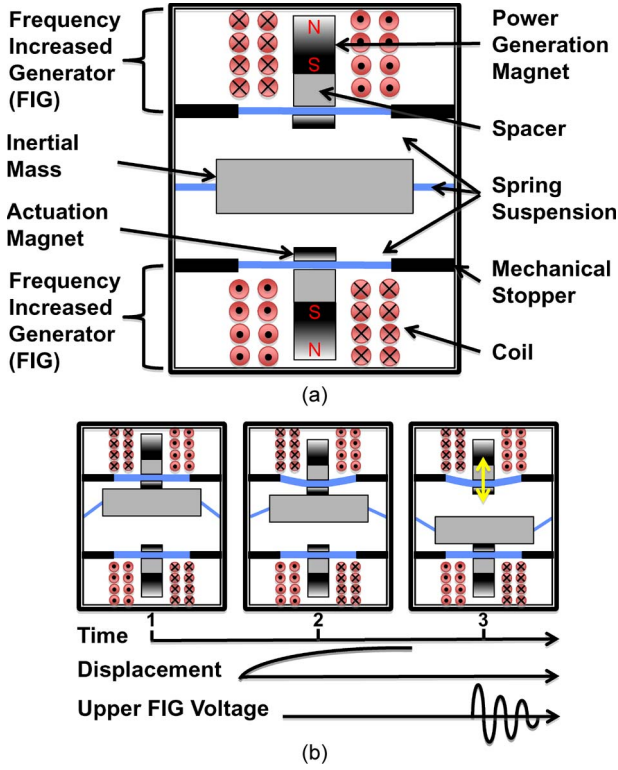


Fig. 2. (a) PFIG architecture. (b) Illustration of the method of operation.

The operation of the PFIG is outlined in Fig. 2(b). The generator operates such that the inertial mass snaps back and forth between the two FIG generators, attaching magnetically. As the inertial mass moves, it pulls the FIG spring along. When the inertial mass approaches the opposing FIG, the magnetic force of attraction begins to increase. As the forces on the FIG/inertial mass system overwhelm the holding magnetic force, the inertial mass detaches and is pulled to the opposing FIG. The freed device now resonates at its high natural frequency, converting the stored mechanical energy in its spring to electrical energy. This process is then repeated in the opposite direction. The main design constraint that needs to be considered is the minimum acceleration at which the PFIG will begin operation. This acceleration is the basis for designing the mechanical system, the size of the mass, the latching force, and the volume.

The PFIG architecture is ideal for two main types of applications: 1) scavenging large-amplitude vibrations that exceed the internal displacement of the generator and 2) scavenging energy using vibrations over a large bandwidth. The converted energy is directly proportional to the frequency with which the mechanical vibrations occur, because the PFIG is capable of producing a certain amount of energy per cycle. The first application space is particularly desirable for MEMS devices where the reduced displacement range can be accommodated much more easily, and the advantages of the microscale can be exploited.

#### A. Modeling of the PFIG

The PFIG generator architecture is composed of three mass–spring–damper systems that influence each other through

two magnetic latching mechanisms. The overall system is shown in Fig. 3(a). The inertial mass  $m_i$  is suspended by a low-stiffness spring  $k_i$ , the main purpose of which is to guide its motion. A damping element with constant  $b_i$  is included to account for the parasitic mechanical losses associated with the inertial mass. The two FIG devices are represented by mass  $m_{fx}$ , spring  $k_{fx}$ , parasitic damper  $b_{fxm}$ , and electrical damper  $b_{fxe}$ . The “ $x$ ” in each of these variables denotes to which FIG the variable belongs, where the FIG on the bottom is henceforth called FIG1 and the FIG above the inertial mass is called FIG2. The electromechanical coupling is modeled as a viscous damping force with damping constant  $b_{fxe}$ .

The displacements of the inertial mass, FIG1, and FIG2 relative to the frame are denoted by  $z(t)$ ,  $s(t)$ , and  $u(t)$ , respectively. A distance of  $Z_{lb}$  and  $Z_{lt}$  separate the rest positions of FIG1 and FIG2 relative to the equilibrium position of the inertial mass. Lastly,  $gap_T$  and  $gap_B$  denote the physical distances between the inertial mass and the top and bottom FIGs, respectively. In this model, each of the three mass elements is given a width  $w m_x$ , which aids in visualization.

When the generator casing is subjected to a time-varying displacement  $y(t)$ , the components inside will respond nonlinearly because of the magnetic forces and discontinuity of the latching mechanism. This means that a closed-form solution for power cannot be computed for the PFIG generator, rather, a time-domain dynamic analysis must be carried out using formulas derived from the device structure. For the purpose of mechanical modeling, the PFIG operation is broken down into three distinct cases. The first case is the situation in which the inertial mass and FIG2 are latched together and moving as a single system, and it is shown in Fig. 3. Symmetrically, Case 2 describes the system when the inertial mass is latched with FIG1. Case 3 accounts for the time during which all three systems are moving separately and in relation to one another, and it is shown in Fig. 4.

#### B. System Dynamics of Cases 1 and 2

The dynamics of Case 1 can be described by two interacting second-order differential equations. The motion of the combined FIG/mass system is given by

$$(m_i + m_{f2})\ddot{u} + b_{f2e}\dot{u} + b_{f2m}\dot{u} + b_i\dot{u} + k_{f2}u + k_i(u + gap_T) = -(m_i + m_{f2})\ddot{y} - F_{mag,1i}. \quad (9)$$

The motion of FIG2 during the time when the mass is latched onto FIG1 is given by

$$m_{f1}\ddot{s} + b_{f1e}\dot{s} + b_{f1m}\dot{s} + k_{f1}s = -m_{f1}\ddot{y} + F_{mag,i1}. \quad (10)$$

The two magnetic forces  $F_{mag,1i}$  and  $F_{mag,i1}$  in (9) and (10) represent the magnetic force that FIG1 exerts on the bottom of the inertial mass and vice versa. These forces are equal in magnitude and opposite in direction. An approximation

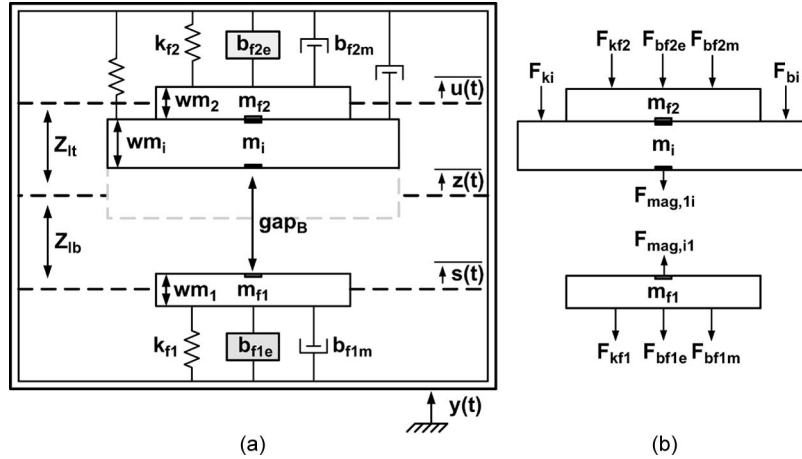


Fig. 3. (a) Mechanical model of the PFIG generator. (b) Force balance on the system when Case 1 is being considered, where the inertial mass is latched onto the top FIG. This case is symmetric to Case 2 when the inertial mass is latched onto the bottom FIG.

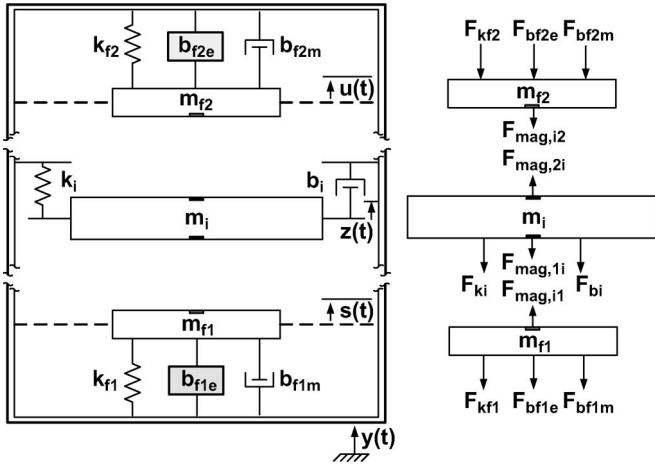


Fig. 4. Illustration of Case 3 when the inertial mass is moving between the two FIG devices.

to the force between two nearby magnetized surfaces is given by

$$F_{mag} = \frac{B^2 A}{2\mu_o} \quad (11)$$

where  $B$  is the magnetic flux density,  $A$  is the area of each surface, and  $\mu_o$  is the permeability of free space ( $\mu_o = 4\pi \times 10^{-7}$  Tm/A). An estimate of the magnetic flux at a point along the central axis of a rectangular magnet is given by [30]

$$B = \frac{B_r}{\pi} \left( \tan^{-1} \left( \frac{WL}{2d\sqrt{4d^2 + W^2 + L^2}} \right) - \tan^{-1} \left( \frac{WL}{2(d+T)\sqrt{4(d+T)^2 + W^2 + L^2}} \right) \right). \quad (12)$$

The flux density is computed as distance  $d$  from a magnet with length  $L$ , width  $W$ , thickness  $T$ , and residual flux density  $B_r$ .

$$d = u - s + [Z_{it} + Z_{ib} - 0.5wm_1 - 0.5wm_2 - wm_i]. \quad (13)$$

In Case 1,  $\dot{z}(t) = \dot{u}(t)$  and  $\ddot{z}(t) = \ddot{u}(t)$ . However, in order to accurately reflect the position of the inertial mass in

terms of  $z(t)$ , an offset is added such that  $z(t) = u(t) + Z_{it} - 0.5wm_2 - 0.5wm_i$ .

While the inertial mass and the FIG are in contact, they each exert an equal and opposite contact (or normal) force on each other. This normal force  $T$  can only be in the direction pointing away from the structure that is applying it. The normal force can never switch directions; it can never be less than zero. This means that when the two structures are no longer in contact, the normal force will become zero. The normal force applied to FIG2 by the inertial mass is given by

$$T = m_{f2}\ddot{u} + b_{f2e}\dot{u} + b_{f2m}\dot{u} + k_{f2}u + F_{mag,2i}. \quad (14)$$

Equation (14) does not work in isolation, but rather, it is coupled with the remaining statements describing the Case 1 system.

Case 2 encompasses the time when the inertial mass is connected to the bottom FIG1. It is symmetric to Case 1 with only sign changes. Therefore, it will not be covered in more detail.

### C. System Dynamics of Case 3

Once the inertial mass leaves either the top or the bottom FIG, all three devices are free to move independently. However, the magnetic forces do influence their motion significantly, particularly when the inertial mass is in close proximity to either of the FIGs, right after separation or just before attachment. The motion of the two FIGs and the inertial mass are given in

$$m_{f2}\ddot{u} + b_{f2e}\dot{u} + b_{f2m}\dot{u} + k_{f2}u = -m_{f2}\ddot{y} - F_{mag,i2} \quad (15)$$

$$m_{f1}\ddot{s} + b_{f1e}\dot{s} + b_{f1m}\dot{s} + k_{f1}s = -m_{f1}\ddot{y} + F_{mag,i1} \quad (16)$$

$$m_i\ddot{z} + b_i\dot{z} + k_i z = -m_i\ddot{y} + F_{mag,2i} - F_{mag,1i}. \quad (17)$$

The magnetic force between the three systems can again be computed using (11) and (12). However, the distance between the FIG magnet and the inertial mass will be different for FIG1

and FIG2. The two distances are a function of the current position of all three systems and are given by

$$d_{2-i} = u - z + [Z_{lt} - 0.5wm_2 - 0.5wm_i] \quad (18)$$

$$d_{1-i} = z - s + [Z_{lb} - 0.5wm_1 - 0.5wm_i]. \quad (19)$$

Case 3 is valid as long as the inertial mass does not make contact with either of the two FIGs. If  $z(t) = u(t) + Z_{lt} - 0.5wm_2 - 0.5wm_i$  or  $z(t) = s(t) - (Z_{lt} - 0.5wm_1 - 0.5wm_i)$ , then Case 3 is no longer valid and the system has transitioned to one of the combined modes. When the inertial mass makes contact with each of the FIG devices, some energy is lost because of the ensuing collision. The impact between the inertial mass and the FIG is modeled as an elastic collision, and (20) and (21) determine the initial and final velocities of the two colliding masses

$$V_{i,\text{final}} = \frac{(C_R + 1)m_{fx}V_{fx} + V_i(m_i - C_R m_{fx})}{m_i + m_{fx}} \quad (20)$$

$$V_{fx,\text{final}} = \frac{(C_R + 1)m_i V_i + V_i(m_{fx} - C_R m_i)}{m_i + m_{fx}}. \quad (21)$$

Here,  $C_R$  is the coefficient of restitution of the materials coming into contact,  $V_i$  and  $V_{fx}$  are the initial velocities of the inertial mass and the appropriate FIG device, respectively, and  $m_i$  and  $m_{fx}$  are the inertial mass and the appropriate FIG mass, respectively. The ensuing velocities of the inertial mass and FIG can now be used to determine the initial velocity condition for the combined system in Case 1 or 2. This is done with conservation of linear momentum in mind.

The PFIG system is simulated using the software tools MATLAB and SIMULINK. A separate SIMULINK model is built for each of the three cases. The interaction between the three cases, the determination of the transition points, the provision of the appropriate initial conditions, and the saving of the data are performed using a control script in MATLAB.

#### D. Power Generation Capability

In order to increase the operating frequency of the PFIG and to decouple it from the low ambient frequency, a mechanical transformation is employed where energy is transferred from the inertial mass to the FIGs. This concept is known as frequency up-conversion, and it was developed at the University of Michigan by Kulah and Najafi [31], [32]. The general principle is shown in Fig. 5. An element is designed to be sensitive to mechanical excitations within a range of low frequencies, and it is excited by displacement at its base. The motion of this low-frequency resonator can then be used to actuate a second higher frequency resonant element (or array of elements). The purpose of this mechanical transformation is to convert the low-frequency large-displacement motion to a higher frequency

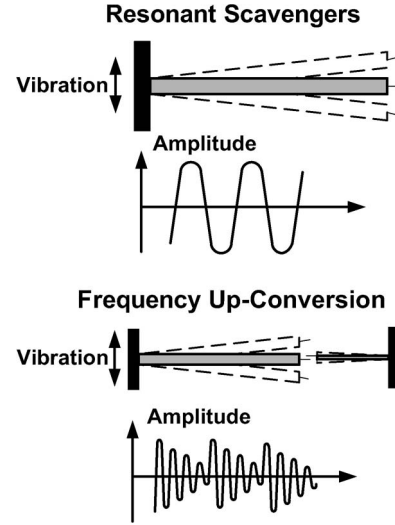


Fig. 5. Illustration describing the frequency up-conversion principle where a low-frequency large-displacement motion is mechanically converted to a higher frequency lower displacement motion.

lower displacement motion. In this manner, the efficiency with which the mechanical energy can then be transformed into electricity is increased. Once energy is stored in the high-frequency mechanical spring, the device is released. The stored mechanical energy is converted to electricity while it vibrates freely.

Calculating the energy converted by the PFIG using the frequency up-conversion method follows the analysis for resonant devices. The distance integral of the damping force  $b_{fe}\dot{u}$  is computed over a full FIG cycle by using (2). The energy converted by each FIG is thus obtained. The integral is taken over the period of the ambient source vibration, to account for the entire time in which the FIG is oscillating after having been actuated. The velocity of the FIG can be represented as

$$\dot{u}(t) = -U_{\text{act}}\omega_{\text{nf}} \frac{e^{-\zeta_{\text{fT}}\omega_{\text{nf}}t}}{\sqrt{1 - \zeta_{\text{fT}}^2}} \sin(\omega_d t) \quad (22)$$

where  $U_{\text{act}}$  is the initial FIG displacement just after release from the inertial mass,  $\omega_{\text{nf}}$  is the natural frequency of the FIG,  $\zeta_{\text{fT}}$  is the combined electrical and parasitic damping ratio of the FIG, and  $\omega_d$  is the damped natural frequency of the FIG

$$\omega_d = \omega_{\text{nf}} \sqrt{1 - \zeta_{\text{fT}}^2}. \quad (23)$$

The result of this integration gives the energy dissipated in the FIG per input vibration cycle. After dividing by the period of the source vibration and multiplying by two to account for the fact that both FIGs will be actuated once per cycle, an equation for total power converted by the PFIG is developed, as shown by (24) at the bottom of the page.

$$P_{\text{total}} = \frac{m_f \zeta_{fe} \omega \omega_{\text{nf}}^3 U_{\text{act}}^2}{1 - \zeta_{\text{fT}}^2} \left[ \frac{1 - e^{-4\pi\zeta_{\text{fT}} \frac{\omega_{\text{nf}}}{\omega}}}{2\zeta_{\text{fT}}\omega_{\text{nf}}} - \frac{e^{-4\pi\zeta_{\text{fT}} \frac{\omega_{\text{nf}}}{\omega}} (2\omega_d \sin(4\pi \frac{\omega_d}{\omega}) - 2\zeta_{\text{fT}}\omega_{\text{nf}} \cos(4\pi \frac{\omega_d}{\omega}))}{4(\zeta_{\text{fT}}^2\omega_{\text{nf}}^2 + \omega_d^2)} \right] \quad (24)$$

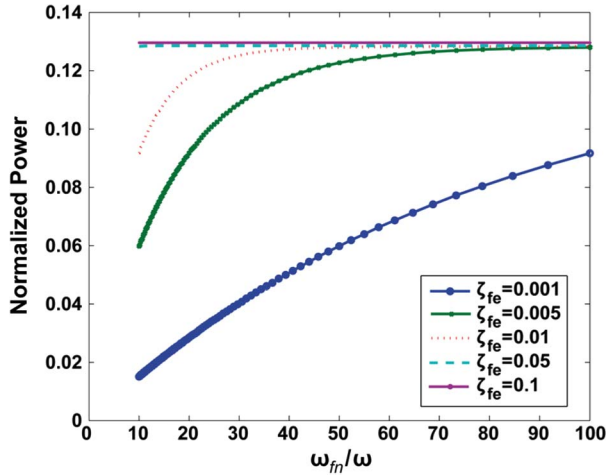


Fig. 6. Simulated performance of the PFIG as a function of the ratio  $\gamma = \omega_{nf}/\omega$  between the natural frequency of the FIG and the ambient vibration frequency  $\omega$  for different damping ratios. Power is normalized to  $m_i\omega^3Y_o^2$ .

Assuming that  $\zeta_{fe}$  (and ignoring parasitics) is large enough such that the FIG motion can be completely damped out per ambient vibration cycle  $2\pi/\omega$ ,  $P_{total}$  can be shown to be

$$P_{total} \sim m_f \gamma^2 \omega^3 U_{act}^2 \quad (25)$$

where  $\gamma = \omega_{nf}/\omega$ . The major optimization goal in the PFIG, and frequency up-conversion schemes in general, is to assure that the reduction in the mass times the reduction in displacement squared is significantly less than the square of the frequency ratio  $\gamma$ . Upon maximizing the initial deflection  $U_{act}$  to be as high as possible in a given volume, for a given  $\zeta_{fe}$ ,  $\gamma$  can be used to maximize the converted potential energy stored in the FIG spring. Shown in Fig. 6 is a simulation where normalized power (normalized to  $m_i\omega^3Y_o^2$ ) is given as a function  $\gamma$ . One can observe that, for a given  $\zeta_{fe}$ , frequency up-conversion can be used to increase the electromechanical coupling and optimally utilize the potential energy transferred during the motional transformation.

#### E. Efficiency and Application of the PFIG

The PFIG has been specifically designed for applications where the vibration amplitude is very large and/or where a response is needed to a broad range of input frequencies. The implications of this can be evaluated by considering the volume figure of merit for a resonant generator, as defined in (7), and by comparing it to the  $F_oM_v$  for the PFIG. A set of practical assumptions is used in evaluating both the resonant generator and the PFIG. Both generators are considered to have a cubic geometry, where one half of the volume is occupied by a mass having a density of  $20 \text{ g/cm}^3$ . The remainder of the space is used for displacement in the resonant generator and the displacement plus additional hardware for the PFIG. This means that  $Z_l$  for the resonant device is set to  $1/4$  of the linear dimension of the given volume, while it is assumed that the PFIG  $gap_T/gap_B$  will not exceed  $1/5$  of the linear dimension for practical configurations. The remainder of the space is apportioned equally between the two FIGs. Equation (5) gives the generated power

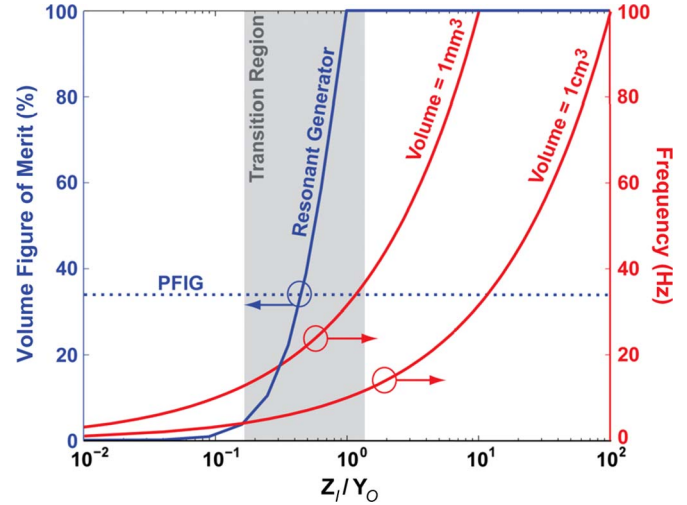


Fig. 7. Simulated volume figure of merit ( $F_oM_v$ ) of a PFIG compared with a resonant generator as a function of  $Z_l/Y_o$ . For a given volume and acceleration, it becomes more efficient to use the PFIG when  $Y_o$  exceeds  $Z_l$ . This happens at an ever-increasing frequency as the volume shrinks, demonstrating the importance of the PFIG for microgenerators.

for the resonant device. The power generated by the PFIG can be calculated using (24), where  $U_{act}$  is ideally equal to  $gap_T/gap_B$  for maximum efficiency. The FIG parameters are optimized by assuming that the  $gap \leq \omega^2 Y_o / \omega_{comb}^2$ , where  $\omega_{comb}$  is the combined resonant frequency of the inertial mass/FIG. In this way,  $k_f$  is first set to maximize the gap, and then,  $m_f$  is set to achieve the desired frequency ratio. The volume of the FIG mass is bounded to  $3/10$  of the volume of the generator in accordance with the geometric confinement discussed previously. If this criterion cannot be achieved, then  $k_f$  is adjusted. The damping and frequency up-conversion ratios are chosen so as to saturate the converted energy. Equation (5) automatically controls the resonant device damping. However, when the displacement of the generator exceeds  $Z_l$ , the constrained damping factor exceeds 1. This invalidates the analysis that led to (5), because an underlying assumption is that the oscillations are cyclic. For this reason, damping is controlled such that the resonant generator will operate with a minimum  $Q$  of 1. When  $Z_l$  is exceeded, the linear dimension of the generator, and hence volume, is increased to accommodate the  $Q$  limitation. Neglecting parasitics, the  $F_oM_v$  values of the two generators are compared in Fig. 7 for an acceleration of  $9.8 \text{ m/s}^2$ . Above  $Z_l/Y_o = 1$ , the resonant generator has an efficiency of 100%, which follows from the way in which  $F_oM_v$  is defined. However, as the input vibration amplitude exceeds  $Z_l$ , the efficiency of the resonant generator rapidly drops. It therefore quickly becomes advantageous to use the PFIG. A transition region is highlighted in gray because, in this space, mathematical modeling and physical implementation diverge for both types of devices. In this region, where  $Z_l/Y_o \sim 0.3-1$ , it becomes more advantageous to utilize the PFIG architecture. For a given acceleration, the frequency of transition is dependent on the volume of the generator. The red curves and the right-hand axis show frequency as a function of  $Z_l/Y_o$  for two different generator volumes. It becomes apparent that the transition point occurs at a higher frequency when the volume is decreased. This observation further emphasizes that the PFIG architecture

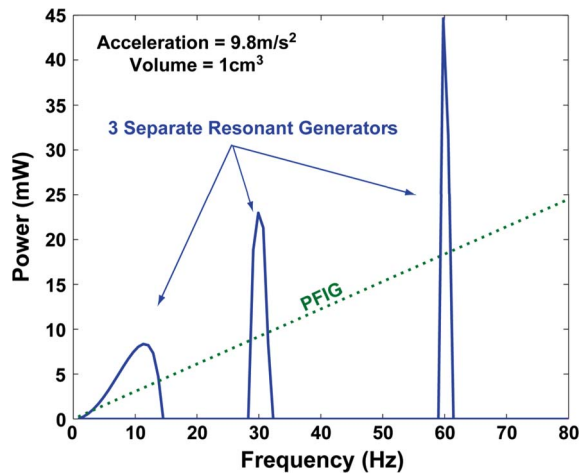


Fig. 8. Simulated frequency response of the PFIG as compared with three resonant generators working at their optimal conditions. The PFIG has an inherent tradeoff between bandwidth for maximum power. However, this allows the PFIG to operate over a large bandwidth.

becomes very important for the miniaturization of vibration harvesters. The vibration amplitude exceeds the generator dimensions for a much greater portion of the frequency range of interest for most applications.

Another important aspect of the PFIG architecture is its wideband nature. A simulation of the frequency response of the PFIG is shown in Fig. 8 alongside three different resonant generators working under optimal conditions. When the application calls for it, power can be traded for bandwidth and the PFIG architecture can be used to scavenge broadband vibrations. The PFIG is shown to work up to 80 Hz in this plot because the simplified power analysis does not take into account the dynamic behavior of the system. The exact frequency range that the generator will cover will depend on the design.

#### IV. ELECTROMAGNETIC PFIG DESIGN AND FABRICATION

A miniature electromagnetic PFIG prototype was developed based on the architecture discussed in the previous section. A target acceleration of 1 g ( $9.8 \text{ m/s}^2$ ) was selected for this design, which is within the range of acceleration levels found on the human body [33], [34]. The PFIG concept is ideally suited for this type of environment since humans produce large-amplitude irregular motion. The generator was designed to operate in the range of  $\leq 10$  Hz. A rendering of the PFIG prototype is shown in Fig. 9. The vertical layout very closely mirrors the theoretical implementation of the device shown in Fig. 2. One can see the FIGs on the top and bottom and the inertial mass in the middle. The generator consists of four separate enclosures bolted together during assembly; the spring suspensions are clamped down in the process.

##### A. Mechanical Design

The dynamic behavior of the PFIG was designed and studied using numerical methods. An initial hand analysis is carried out to select the starting configuration for many of the parameters. Design decisions are primarily based on desired volume, vibration environment, availability of materials, and fundamental

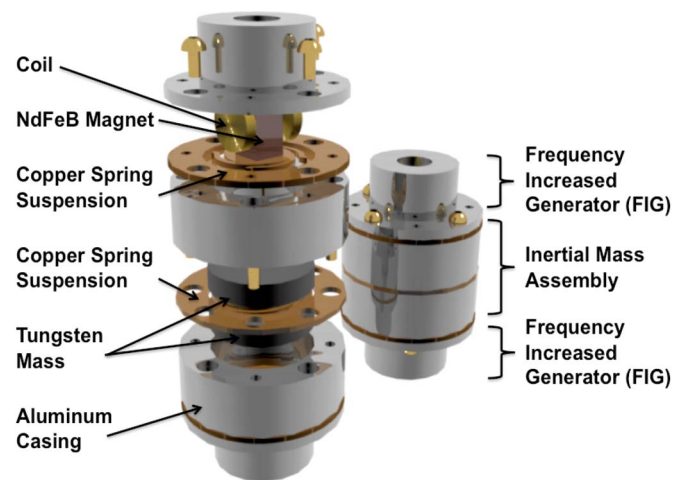


Fig. 9. Exploded view of the electromagnetic PFIG showing the structure of the device, components, and assembly.

limits on various parameters. After this first-order analysis, numerical simulations are carried out to find a stable and reliable configuration for the entire PFIG.

Having determined the values for the mechanical parameters, the components themselves can then be designed to meet the specifications that are required of them. Both the inertial mass and the FIG spring are made out of copper. Copper is easily micromachined, and it is a readily available material. A crab leg design was used for the FIG spring and a meandering fixed-fixed beam was used in the design of the inertial mass spring. The geometry of the beams was designed using ANSYS. Spring arms are fixed on the sides, and they terminate in the middle with a large pad ( $3.5 \times 3.5 \text{ mm}$ ) where either magnets or the inertial mass is attached. The crab-leg springs have four legs, each of which has two sections of lengths 5.1 and 5.8 mm, width of  $440 \mu\text{m}$ , and thickness of  $127 \mu\text{m}$ . In order to mitigate stress, right angles are eliminated from the layout. The inertial mass spring has two meandering arms of 15.8-mm total length,  $440\text{-}\mu\text{m}$  width, and  $125\text{-}\mu\text{m}$  thickness.

##### B. Electrical Design

An optimized design of the electromagnetic transduction system was developed using the software package Ansoft Maxwell. Only single coil/magnet configurations were considered. An arrangement where a cylindrical magnet, poled along the  $z$ -axis, is moved perpendicular to the plane of a coil underneath was found to be the most efficient. This result is confirmed by a study where coil/magnet topologies were studied numerically [35]. Transient 3-D simulations were performed. A nominal configuration was chosen, and the effects of depth, gap, offset, and magnet dimensions on the induced voltage were studied one at a time.

A cylindrical magnet with a diameter of 3.175 mm and a thickness of 4.75 mm was used. The coil had a width of 2 mm and a length of 3.175 mm. The nominal gap was 0.5 mm. The magnet was initially positioned exactly on top of the coil plane. The coil resistance was set to  $240 \Omega$ , and the magnet was given a sinusoidal displacement of 0.4 mm at a frequency of 200 Hz, values extracted from the mechanical model. Increasing the

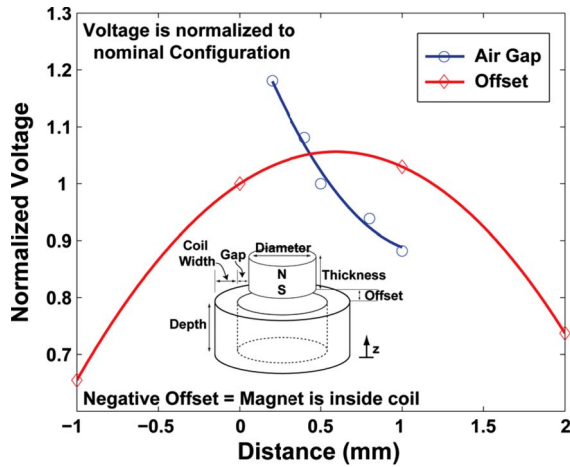


Fig. 10. Perpendicular coil arrangement simulations using Maxwell 3-D. The normalized induced voltage (normalized to nominal configuration) is shown as a function of coil/magnet offset and air gap. Coil/magnet topology is shown in the figure insert.

size of the magnet produced higher voltages, as did increasing the coil depth and decreasing the coil width. Given a certain volume, optimizing the offset and the gap between the coil and the magnet was found to be the most important design aspect. Fig. 10 shows results of simulations varying the coil/magnet air gap and offset parameters. The induced voltage is normalized to the nominal configuration in order to show the relative importance of these parameters. The data are fitted using second-order polynomials. Changing the air gap from 0.2–1 mm reduced the voltage by 34%. Additionally, changing the offset by setting the magnet  $\pm 1$  mm from its optimal position yielded a  $> 30\%$  reduction in the voltage. The most remarkable result was that the optimal position was slightly above the coil plane at 0.6 mm (when using the nominal values for the other parameters).

### C. Fabrication

The PFIG prototype is fabricated using a hybrid approach where standard lithographic techniques are combined with traditional machining and assembly. The springs for both the FIG and the inertial mass are fabricated out of a  $127\text{-}\mu\text{m}$ -thick copper alloy 110. The copper sheets are mounted on carrier silicon wafers using photoresist, lithographically patterned, and immersion etched in  $\text{FeCl}_3$  at  $45^\circ\text{C}$ . Fig. 11(a) shows a fabricated FIG spring. The FIG spring assembly is made by bonding a 2.4-mm-thick and 4.76-mm-diameter rare earth neodymium iron boron, NdFeB, magnet to the spring on top of a  $1 \times 1 \times 0.5$  mm plastic spacer. Another cylindrical magnet with diameter of 1.15 mm and thickness of 0.5 mm is bonded on the other side of the FIG spring for latching and actuation purposes. The neodymium magnets are grade N42 ( $B_r = 1.3$  T). The FIG spring assembly can be seen in Fig. 11(b).

Coils for the FIGs are wound from 44AWG enameled copper wire. The coil was wound on a specially designed and manufactured bobbin. The bobbins are made out of aluminum using a computer-controlled mill. Microscale topology left by the milling process sometimes penetrated the enamel of the wire during coil winding and produced shorting between the coil



Fig. 11. Photographs of fabricated PFIG components and completed generator. (a) FIG spring on top of U.S. quarter. (b) FIG spring assembly. (c) Machined bobbins on top of a U.S. quarter and wound coil. (d) Assembled FIG casing with a coil fixed inside. (e) Inertial mass assembly. (f) Inertial mass inside a partially opened casing. (g) Completed PFIG alongside a standard AA battery.

and the generator body. Therefore, subsequent versions of the bobbins were made out of polyvinyl chloride to improve repeatability. The bobbins had an inner diameter of 5.54 mm and a sidewall thickness of  $300\ \mu\text{m}$ . The sidewall thickness adds to the coil/magnet gap and should be minimized. Fig. 11(c) shows a photograph of the machined bobbins and wound coil. The coil and bobbin are aligned and fixed inside the FIG compartment using a single 000–120 screw in the center [Fig. 11(d)].

The inertial mass is made from tungsten carbide, which is a very dense material,  $14.7\text{--}14.9\ \text{g/cm}^3$ , and results in a compact mass. A 10-mm-diameter rod is machined using electric discharge machining, after which it is ground down for planarization. Two pieces, each with a thickness of 3.9 mm, are bonded using cyanoacrylate on each side of the spring suspension atop a 1-mm spacer. An alignment jig is used

center the mass pieces on the spring. The inertial mass assembly is shown in Fig. 11(e).

The generator casing is milled out of aluminum. It has a 1-mm sidewall running throughout. The most intricate parts are the inertial mass enclosures, which contain all of the taps and bore used to secure and fasten the entire generator together. Fig. 11(f) shows the inertial mass and the generator casing components. Additionally, the FIG compartment lip, which is used to secure the FIG to the generator body, has an inner diameter smaller than the inertial mass. In this way, the compartment lip acts as a shock stop to prevent damage of the FIG spring. Fig. 11(g) shows the assembled PFIG next to a standard AA-sized battery.

V. RESULTS

The PFIG generator is tested using an Unholtz–Dickie 5PM electrodynamic shaker controlled by a UD MA-630 transducer calibration control system. Table I shows a complete characterization of the fabricated PFIG. Initial testing was performed to characterize the FIG devices. Waveform traces of the generated output voltage are used to determine the natural frequency of the device, as well as to investigate the parasitic damping and electromechanical coupling of the system using a technique discussed in [17].

The PFIG is tested at 1 g, and the acceleration level for which it was designed. The minimum frequency at which the generator can be tested accurately is 10 Hz due to limitations associated with the vibration test system. Each FIG is loaded with a 220-Ω resistor. The PFIG generator is tested in the *x*-axis (horizontal direction). This initial design does not account for gravity, and in order to eliminate this bias, the shaker table is inclined by 90°. Fig. 12(a) shows voltage waveforms from the top and bottom FIGs. On the left side of the figure, simulation results are shown for a similarly configured device using extracted damping parameters from Table I. On the right side are the measured waveforms recorded during testing. Fig. 12(b) is a zoomed-in view of the waveforms in Fig. 12(a). The simulation results predict the experimental performance quite closely. One can see that the decaying oscillations for both the simulated and measured waveforms reach a max/min of  $\pm 100$  mV<sub>ppk</sub>. Of course, the measured waveforms have voltage spikes each time the inertial mass latches and makes contact, as well as some ringing. The reason for this can be seen in Fig. 2(a). The actuation magnet sits above the FIG spring and above the mechanical stopper. This means that, as the inertial mass makes contact, it can rapidly compress the FIG spring and suddenly stop when it reaches the mechanical stopper. As the inertial mass stops, the FIG can separate, provided the right conditions, and this results in the ringing in the waveform. The complete effects of the mechanical stopper, as well as the ability to separate into three degrees of freedom after reaching it, are not modeled accurately in the simulations. Since these effects do not directly define the operation of the device, all of these complex interactions are approximated using an inelastic collision, as was discussed in Section III.

The voltage traces in Fig. 12(a) show that the FIGs are not working symmetrically. Heavy mechanical damping in FIG1

TABLE I  
ELECTROMAGNETIC PFIG SUMMARY

Coil Turns, N	1200
Coil Resistance	220Ω
Coil Inductance	8.4 mH
Spring Constant, $k_f$	612 N/m
Mass, $m_f$	0.396 g
Natural Frequency, $f_n$	200 Hz
Magnet Types	NdFeB
Actuation Magnet Diameter	1.1 mm
Actuation Magnet Thickness	0.5 mm
Generation Magnet Diameter	4.76 mm
Generation Magnet Thickness	2.4 mm
$Q_T$	49.5
$Q_e$	99
$Q_m$	99
<b>PFIG</b>	
Inertial Mass, $m_i$	9.3 g
Spring Constant, $k_i$	150 N/m*
Actuation Gap, $gap_T/gap_B$	0.35 mm
Internal Volume	2.12 cm <sup>3</sup>
Total Volume	3.75 cm <sup>3</sup>
Avg. Power (9.8m/s <sup>2</sup> , 10Hz)	13.6 μW
Peak Power (9.8m/s <sup>2</sup> , 10Hz)	163 μW
Cut-Off Frequency (9.8m/s <sup>2</sup> )	65 Hz
Volume Figure of Merit, $F_oM_v$ (9.8m/s <sup>2</sup> )	0.068%
Bandwidth Fig. of Merit, $F_oM_{BW}$ (9.8m/s <sup>2</sup> )	0.375%

\*Simulated Value

causes the large asymmetry in the measured results. This is caused by friction between the magnet and the inner sidewall of the coil bobbin due to misalignment. However, one can see asymmetry between the overall waveforms both from the measured results and the simulations. The reason for this non-symmetric behavior is explained by Fig. 12(c), which shows a simulation of the FIG and inertial mass movement during operation. The middle curve represents the inertial mass. One can see that the release point depends heavily on the overall system dynamics, the magnetic interaction near the point of release, as well as immediately after release. Therefore, the gap at which the normal force on the FIG becomes zero will vary each cycle, and the FIGs will operate asymmetrically.

The performance of the PFIG was evaluated over a range of frequencies and accelerations (Fig. 13). The minimum acceleration of the PFIG is 1 g, and the maximum acceleration of the shaker table is 2 g. The frequency of the vibration is changed from 10 Hz up to when the PFIG ceased to operate at 65 Hz. The

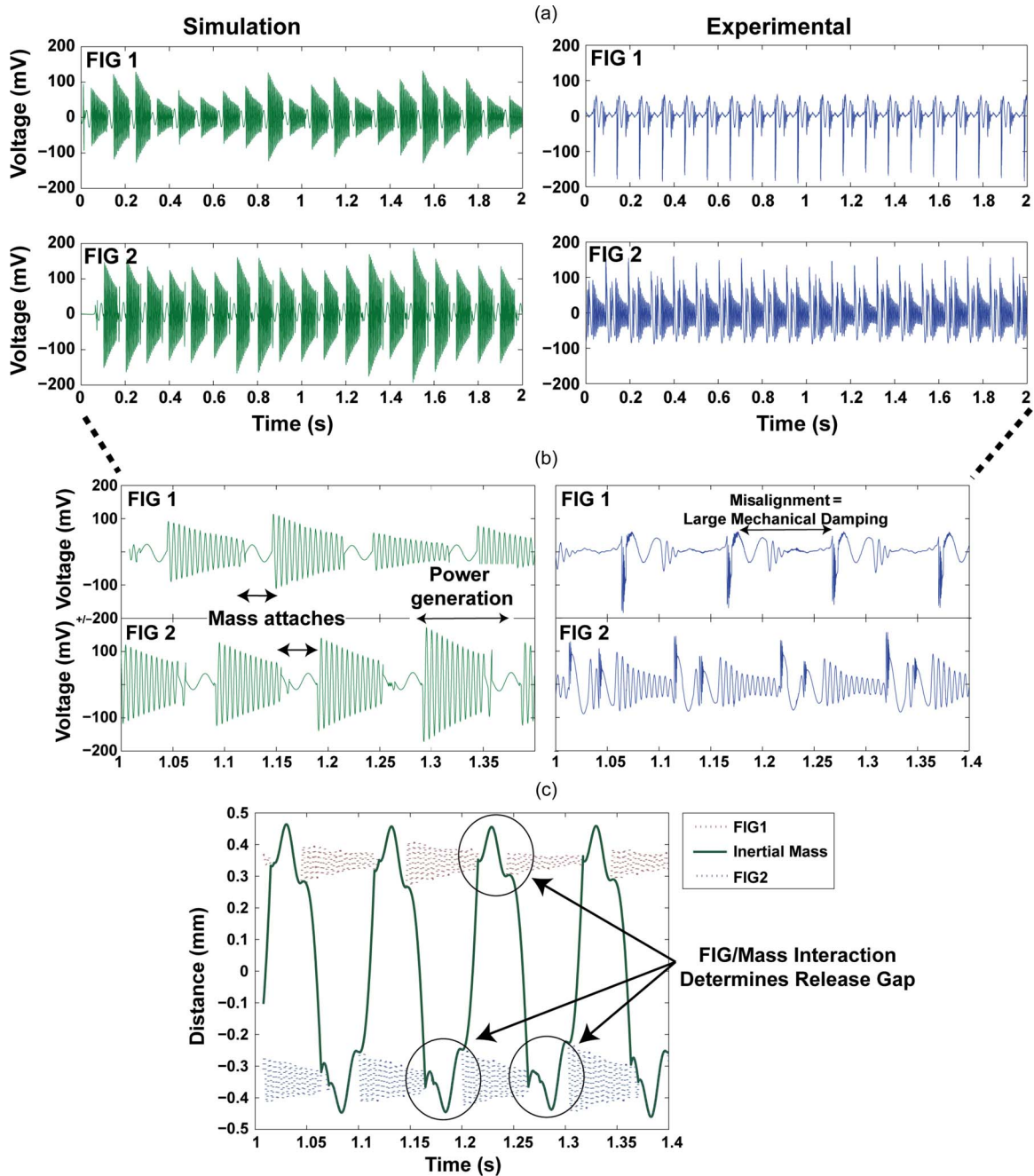


Fig. 12. (Left side) Simulated and (right side) experimental voltage waveforms of the FIGs showing the PFIG operation from 1-g acceleration at 10 Hz. (a) Two-second voltage trace. (b) Close-up of the simulated and measured voltage waveforms. (c) Simulation showing the FIG and inertial mass motion during operation. The complex interaction that occurs during latching/release causes asymmetry of the voltage waveforms during operation.

average power that could be generated from a 1-g vibration at 10 Hz was  $13.6 \mu\text{W}$ . Defining bandwidth as the  $-3\text{-dB}$  reduction in power and the center frequency to be 10 Hz, the PFIG has a bandwidth of 55 Hz.

## VI. DISCUSSION

The performance of the electromagnetic PFIG is a significant advancement to the state-of-the-art in vibration scavengers. Due to the way in which the PFIG operates, producing decaying oscillations, this paper has mainly dealt with the average power over large samples of collected data. Most scavengers

are benchmarked to their peak power-generating capability. That makes sense if the devices were operating resonantly and producing symmetric periodic output voltage waveforms. Then, the peak power is close to the RMS power, and this benchmarking is appropriate. In many other cases, including the PFIG, it is more appropriate to use average power. The  $F_o M_v$  for the PFIG is computed using average power generated by the device, and it is shown in Fig. 14. The  $F_o M_v$  for the PFIG is computed for a range of recorded operating frequencies. The performance of the PFIG can be seen alongside the state-of-the-art in the energy harvesting field [36]–[70]. The PFIG generator constitutes a significant improvement in efficiency for low-frequency

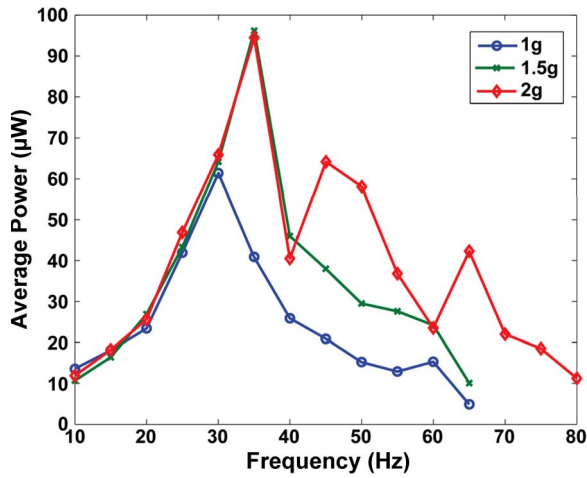


Fig. 13. Measured frequency response of the PFIG generator at three different acceleration levels.

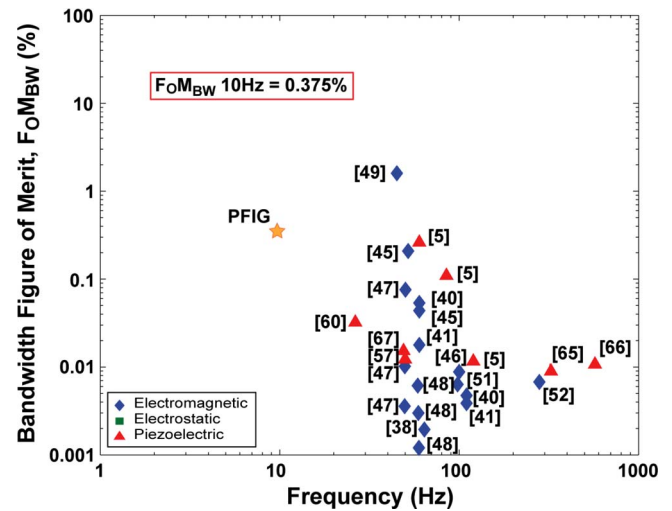


Fig. 15. Bandwidth figure of merit ( $F_oM_{BW}$ ) comparison of the PFIG generator to the state-of-the-art in vibration scavengers.

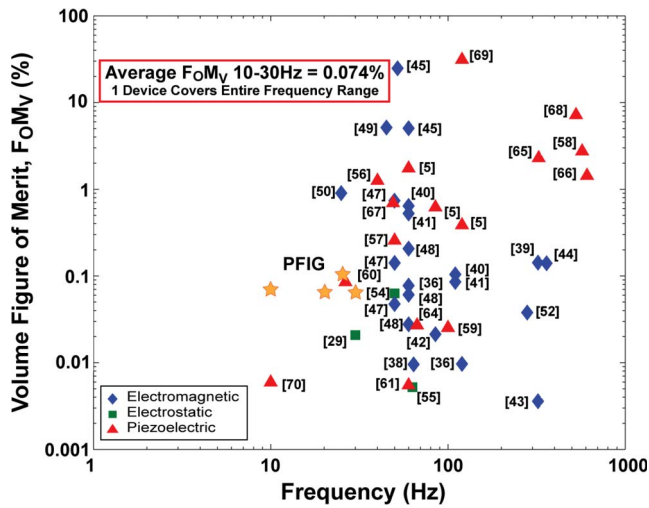


Fig. 14. Volume figure of merit ( $F_oM_v$ ) comparison of the PFIG generator to the state-of-the-art in vibration scavengers.

(< 20 Hz) scavengers. The large operating range of the PFIG is unprecedented, but this is not an aspect which is illuminated easily by the  $F_oM_v$  plot. For this reason, the bandwidth figure of merit (8) is computed and plotted along with the state of the art, taking into account its bandwidth, in Fig. 15. The center frequency used for the calculations is the main frequency of interest, which, in this case, is the lowest frequency at which the PFIG can operate. It should be noted that bandwidth data are not readily available in publications. For many of the published works, the bandwidth of the generator was estimated from publication figures and other data, in each case, erring on the side to favor to the device in the publication. The PFIG has the best  $F_oM_{BW}$  of all vibration harvesters published to date, except for one effort that uses active frequency tuning.

### A. Performance Enhancements Through Structural Modifications

The performance of the PFIG is a significant advancement in scavenging low-frequency vibrations. However, a number of improvements can be made to future designs of the PFIG

architecture. The first set of enhancements constitutes structural changes that can be made to the PFIG in order to improve the system dynamics and to produce higher output power. A significant amount of energy is being lost to frictional damping. This energy loss both alters the system dynamics, and when it happens inside the FIG, it also is a direct loss mechanism of the electrical to mechanical energy conversion. Since the inertial mass is suspended in the middle, the whole assembly is susceptible to torsional motion. The same issue is present in the design of the FIG spring assembly where the magnet acts as an eccentric mass. These challenges are magnified by the horizontal testing because gravity is acting on these components. A related issue is the alignment and placement of the FIG spring relative to the coil and other FIG components. The bolts that secure the FIG were designed to act like alignment pins; however, the tolerances of the various components (particularly the ones manufactured by nonlithographical means) made the resolution of this alignment scheme poor.

These structural issues, although unfortunate, can easily be remedied in the future. Suspending the inertial mass and the FIG magnet from both sides will greatly reduce out-of-axis and bending motion. Alignment of the FIG components can also be improved quite trivially, by simply having the clamping mechanism on the top, such that alignment and clamping can be performed together.

### B. Improved Power Conversion and Efficiency

Significantly improving the electrical damping of the system is needed for higher efficiency. There is room for improvement beyond the single coil/magnet topology used in this work. More sophisticated magnetic circuits can be developed which confine and route the flux [33], [45] as opposed to letting it spread out. These require careful design so as not to introduce significant eddy currents and hysteresis losses that limit the efficiency. Solutions such as combining transduction mechanisms can also be explored. Because of the nonresonant operation, as well as the transfer of energy from the inertial mass to the FIG, the PFIG is not limited in terms of  $\zeta_e$  in the same way that a

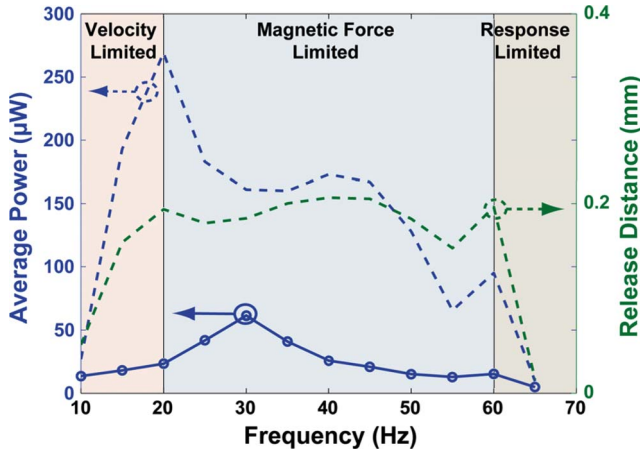


Fig. 16. Frequency response comparison simulated system (dotted lines) and the performance of the PFIG at 1 g. Plot also shows the release distance as a function of frequency.

resonant generator is. In fact, the mechanical parasitics should be reduced to an absolute minimum, while  $\zeta_e$  is increased as much as possible.

### C. Minimum Acceleration and Bandwidth Considerations

The PFIG generator undergoes several distinct modes of operation, as shown in Fig. 16. As the frequency is increased, the generator transitions from a velocity limited region to one where its operation is limited by the physical constraints of the design ( $gap_T/gap_B$ ) as well as the latching force and, finally, to a cutoff region where the system is too slow to respond to the incoming vibrations. These regions are shown in Fig. 16, and they can be identified in both the simulated response curve and the measured data. Additionally, the average release gap or the distance the FIG is actuated before it detaches from the inertial mass is shown. This is an average over the entire data set of a particular frequency, because variations will occur due to the dynamic behavior of the system. In the velocity-limited region, the system response is dictated by the increasing frequency (and, hence, velocity). As the frequency goes up, the inertia of the FIG gradually increases and counteracts the spring force to push the release gap further and further up. The first resonant peak amplifies this effect by providing more energy for the system. The first resonant peak is determined by the inertial mass/suspension natural frequency. Past this first resonance, the effect of the FIG inertia, pushing the release distance higher and higher, saturates and the unlatching point becomes limited by the FIG spring force exceeding the magnetic latching force. The average power drop is a result of the inertial mass not being able to track the vibration. This means that each FIG is actuated fewer than once per period, with the number of actuations depending on the transient dynamics of the system. The onset of the final phase is governed by the natural frequency of the combined FIG/inertial mass resonator  $f_{nc}$ , which is approximately 45 Hz for the system in Fig. 16. The force transmissibility [71] quickly starts to decrease, and eventually, the deflection makes it so the normal force cannot reach zero. Another possible outcome is that the inertial mass releases the FIG, but it can never deflect enough to latch on again.

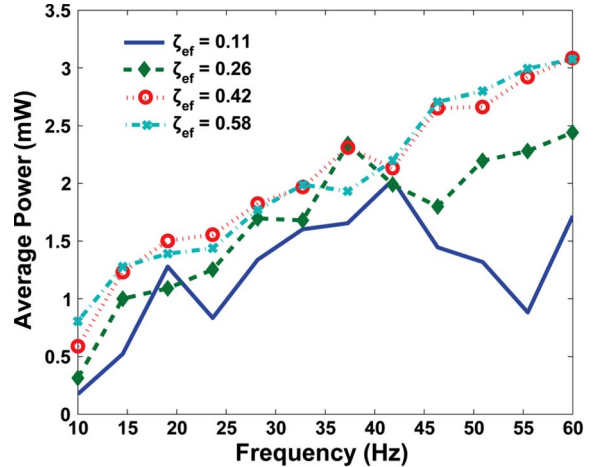


Fig. 17. Simulation showing average power versus electrical damping ratio of the FIG.

One sure way of increasing the bandwidth and the power generation of the PFIG is to increase the electrical damping. Fig. 17 shows a simulation demonstrating this. In actuality, the mechanical performance remains the same and the bandwidth of the PFIG is not changing. However, the amount of energy coupled into the FIGs largely goes to waste at higher frequencies, because before the oscillation of the FIG can decay, the inertial mass latches on again. By increasing the electro-mechanical coupling, more of the energy can be converted before the next cycle. Even though the FIG does not actuate every cycle at higher frequencies, there are enough latching events to keep pushing the power output higher. Once again, this evidence supports the need for sophisticated electromechanical transduction for proper PFIG operation.

## VII. CONCLUSION

This paper has introduced a new vibration harvester architecture called the PFIG. A theoretical framework for analysis of the PFIG architecture was presented. The device dynamics are modeled by considering the structure during three cases of operation that transition between 2- and 3-DOF magnetically coupled systems. An analysis was carried out to show in which ambient conditions is it better to choose the PFIG over a resonant harvester. The PFIG offers better efficiency than resonant devices when the vibration amplitude exceeds the internal displacement limit of the microgenerator, as well as when a large bandwidth is required at low frequency. The design, fabrication, and testing of the first electromagnetic PFIG power scavenger were discussed. The average power that can be generated from an input acceleration of 1 g applied at 10 Hz is 13.6  $\mu$ W. The device is able to operate over a large frequency range and has a 3-db bandwidth of 55 Hz. A volume figure of merit of 0.068% is achieved at 10 Hz, and a bandwidth figure of merit of 0.375% is achieved with a center frequency of 10 Hz. These results set the state-of-the-art in the field when considering very low (< 20 Hz) vibration scavengers.

## ACKNOWLEDGMENT

The authors would like to thank Sandia National Laboratories for the fellowship support.

## REFERENCES

- [1] D. Dunn-Rankin, E. N. M. Leal, and D. C. Walther, "Personal power systems," *Prog. Energy Combust. Sci.*, vol. 31, pp. 422–465, 2005.
- [2] J. D. Morse, "Micro-fuel cell power sources," *Int. J. Energy Res.*, vol. 31, no. 6/7, pp. 576–602, May 2007.
- [3] Z. Chunbo and K. Najafi, "Fabrication of thick silicon dioxide layers for thermal isolation," *J. Micromech. Microeng.*, vol. 14, no. 6, pp. 769–774, Jun. 2004.
- [4] M. Hatler, D. Gurganious, and M. Ritter, "Perpetual power solutions for wireless sensor networks," ON World Inc., 2008. [Online]. Available: <http://www.onworld.com/power/index.html>
- [5] S. Roundy, "Energy scavenging for wireless sensor nodes with a focus on vibration to electricity conversion," Ph.D. dissertation, Univ. California Berkeley, Berkeley, CA, 2003.
- [6] W. Glatz, E. Schwyter, L. Durrer, and C. Hierold, "Bi<sub>2</sub>Te<sub>3</sub>-based flexible micro thermoelectric generator with optimized design," *J. Microelectromech. Syst.*, vol. 18, no. 3, pp. 763–772, Jun. 2009.
- [7] F. Liu, A. Phipps, S. Horowitz, N. Khai, L. Cattafesta, T. Nishida, and M. Sheplak, "Acoustic energy harvesting using an electromechanical Helmholtz resonator," *J. Acoust. Soc. Amer.*, vol. 123, no. 4, pp. 1983–1990, Apr. 2008.
- [8] A. S. Holmes, H. Guodong, and K. R. Pullen, "Axial-flux permanent magnet machines for micropower generation," *J. Microelectromech. Syst.*, vol. 14, no. 1, pp. 54–62, Feb. 2005.
- [9] S. Roundy, P. K. Wright, and J. Rabaey, "A study of low level vibrations as a power source for wireless sensor nodes," *Comput. Commun.*, vol. 26, no. 11, pp. 1131–1144, Jul. 2003.
- [10] P. D. Mitcheson, E. M. Yeatman, G. K. Rao, A. S. Holmes, and T. C. Green, "Energy harvesting from human and machine motion for wireless electronic devices," *Proc. IEEE*, vol. 96, no. 9, pp. 1457–1486, Sep. 2008.
- [11] S. P. Beeby, M. J. Tudor, and N. M. White, "Energy harvesting vibration sources for microsystems applications," *Meas. Sci. Technol.*, vol. 17, no. 12, pp. 175–195, Dec. 2006.
- [12] T. Galchev, "Energy scavenging from low frequency vibrations," Ph.D. dissertation, Elect. Eng., Univ. Michigan, Ann Arbor, MI, 2010.
- [13] C. B. Williams, C. Shearwood, M. A. Harradine, P. H. Mellor, T. S. Birch, and R. B. Yates, "Development of an electromagnetic micro-generator," *Proc. Inst. Elect. Eng.—Circuits, Devices Syst.*, vol. 148, no. 6, pp. 337–342, Dec. 2001.
- [14] C. Shearwood and R. B. Yates, "Development of an electromagnetic micro-generator," *Electron. Lett.*, vol. 33, no. 22, pp. 1883–1884, Oct. 1997.
- [15] S. Meninger, T. O. Mur-Miranda, R. Amirtharajah, A. Chandrakasan, and J. Lang, "Vibration-to-electric energy conversion," in *Proc. Int. Symp. Low Power Electron. Des.*, 1999, pp. 48–53.
- [16] S. Meninger, J. O. Mur-Miranda, R. Amirtharajah, A. Chandrakasan, and J. H. Lang, "Vibration-to-electric energy conversion," *IEEE Trans. Very Large Scale Integr. (VLSI) Syst.*, vol. 9, no. 1, pp. 64–76, Feb. 2001.
- [17] T. Galchev, H. Kim, and K. Najafi, "Non-resonant bi-stable frequency increased power generator for low-frequency ambient vibration," in *Proc. 15th Int. Conf. Solid-State Sens., Actuators, Microsyst., TRANSDUCERS*, Denver, CO, 2009, pp. 632–635.
- [18] T. Galchev, H. Kim, and K. Najafi, "A parametric frequency increased power generator for scavenging low frequency ambient vibrations," in *Proc. Eurosensors XIII*, Lausanne, Switzerland, 2009, pp. 1439–1442.
- [19] S. Beeby, M. Tudor, R. Torah, S. Roberts, T. O'Donnell, and S. Roy, "Experimental comparison of macro and micro scale electromagnetic vibration powered generators," *Microsyst. Technol.*, vol. 13, no. 11/12, pp. 1647–1653, Jul. 2007.
- [20] P. D. Mitcheson, T. C. Green, E. M. Yeatman, and A. S. Holmes, "Architectures for vibration-driven micropower generators," *J. Microelectromech. Syst.*, vol. 13, no. 3, pp. 429–440, Jun. 2004.
- [21] D. Paci, M. Schipani, V. Bottarel, and D. Miatton, "Optimization of a piezoelectric energy harvester for environmental broadband vibrations," in *Proc. 15th IEEE ICECS*, 2008, pp. 177–181.
- [22] E. Reilly, L. Miller, R. Fain, and P. K. Wright, "A study of ambient vibrations for piezoelectric energy conversion," in *Proc. PowerMEMS*, Washington, DC, 2009, pp. 312–315.
- [23] T. von Buren, P. Lukowicz, and G. Troster, "Kinetic energy powered computing—An experimental feasibility study," in *Proc. 7th IEEE Int. Symp. Wearable Comput.*, 2003, pp. 22–24.
- [24] M. Ferrari, V. Ferrari, D. Marioli, and A. Taroni, "Modeling, fabrication and performance measurements of a piezoelectric energy converter for power harvesting in autonomous microsystems," *IEEE Trans. Instrum. Meas.*, vol. 55, no. 6, pp. 2096–2101, Dec. 2006.
- [25] E. S. Leland and P. K. Wright, "Resonance tuning of piezoelectric vibration energy scavenging generators using compressive axial preload," *Smart Mater. Struct.*, vol. 15, no. 5, pp. 1413–1420, Oct. 2006.
- [26] S. Roundy and Y. Zhang, "Toward self-tuning adaptive vibration-based microgenerators," in *Proc. Smart Struct., Devices, Syst. II*, Sydney, Australia, 2005, pp. 373–384.
- [27] C. Eichhorn, F. Goldschmidtboeing, Y. Porro, and P. Woias, "A piezoelectric harvester with an integrated frequency-tuning mechanism," in *Proc. PowerMEMS*, Washington, DC, 2009, pp. 45–48.
- [28] I. Sari, T. Balkan, and H. Kulah, "An electromagnetic micro power generator for wideband environmental vibrations," *Sens. Actuators A, Phys.*, vol. 145/146, pp. 405–413, 2008.
- [29] P. Miao, P. D. Mitcheson, A. S. Holmes, E. M. Yeatman, T. C. Green, and B. H. Stark, "MEMS inertial power generators for biomedical applications," *Microsyst. Technol.*, vol. 12, no. 10, pp. 1079–1083, Aug. 2006.
- [30] M. Mizuno and D. G. Chetwynd, "Investigation of a resonance microgenerator," *J. Micromech. Microeng.*, vol. 13, no. 2, pp. 209–216, Mar. 2003.
- [31] H. Kulah and K. Najafi, "Energy scavenging from low-frequency vibrations by using frequency up-conversion for wireless sensor applications," *IEEE Sensors J.*, vol. 8, no. 3, pp. 261–268, Mar. 2008.
- [32] H. Kulah and K. Najafi, "An electromagnetic micro power generator for low-frequency environmental vibrations," in *Proc. MEMS*, 2004, pp. 237–240.
- [33] T. von Buren and G. Troster, "Design and optimization of a linear vibration-driven electromagnetic micro-power generator," *Sens. Actuators A, Phys.*, vol. 135, no. 2, pp. 765–775, Apr. 2007.
- [34] C. R. Saha, T. O'Donnell, N. Wang, and P. McCloskey, "Electromagnetic generator for harvesting energy from human motion," *Sens. Actuators A, Phys.*, vol. 147, no. 1, pp. 248–253, Sep. 2008.
- [35] D. Spreemann, D. Hoffmann, B. Folkmer, and Y. Manoli, "Numerical optimization approach for resonant electromagnetic vibration transducer designed for random vibration," *J. Micromech. Microeng.*, vol. 18, no. 10, p. 104 001, Oct. 2008.
- [36] W. J. Li, T. C. H. Ho, G. M. H. Chan, P. H. W. Leong, and W. H. Yung, "Infrared signal transmission by a laser-micromachined, vibration-induced power generator," in *Proc. 43rd IEEE Midwest Symp. Circuits Syst.*, 2000, pp. 236–239.
- [37] N. N. H. Ching, H. Y. Wong, W. J. Li, P. H. W. Leong, and Z. Wen, "PCB integrated micro-generator for wireless systems," in *Proc. Int. Symp. Smart Struct.*, Hong Kong, 2000, pp. 876–879.
- [38] W. J. Li, Z. Wen, P. K. Wong, G. M. H. Chan, and P. H. W. Leong, "A micromachined vibration-induced power generator for low power sensors and robotic systems," in *Proc. World Autom. Congr. 8th Int. Symp. Robot. Appl.*, Maui, HI, 2000.
- [39] M. El-hami, P. Glynn-Jones, N. M. White, M. Hill, S. Beeby, E. James, A. D. Brown, and J. N. Ross, "Design and fabrication of a new vibration-based electromechanical power generator," *Sens. Actuators A, Phys.*, vol. 92, no. 1–3, pp. 335–342, Aug. 2001.
- [40] N. N. H. Ching, H. Y. Wong, W. J. Li, P. H. W. Leong, and Z. Wen, "A laser-micromachined multi-modal resonating power transducer for wireless sensing systems," *Sens. Actuators A, Phys.*, vol. 97/98, pp. 685–690, Apr. 2002.
- [41] N. N. H. Ching, H. Y. Wong, W. J. Li, P. H. W. Leong, and Z. Wen, "A laser-micromachined vibration to electrical power transducer for wireless sensing systems," in *Proc. 11th Int. Conf. Solid-State Sens. Actuators*, Munich, Germany, 2001, vol. 1, pp. 38–41.
- [42] J. M. H. Lee, S. C. L. Yuen, W. J. Li, and P. H. W. Leong, "Development of an AA size energy transducer with micro resonators," in *Proc. ISCAS*, Bangkok, Thailand, 2003, pp. 876–879.
- [43] P. Glynn-Jones, M. J. Tudor, S. P. Beeby, and N. M. White, "An electromagnetic, vibration-powered generator for intelligent sensor systems," *Sens. Actuators A, Phys.*, vol. 110, no. 1–3, pp. 344–349, Feb. 2004.
- [44] S. Beeby, J. Tudor, R. Torah, E. Koukharenko, S. Roberts, T. O'Donnell, and S. Roy, "Macro and micro scale electromagnetic kinetic energy harvesting generators," in *Proc. DTIP MEMS MOEMS*, Stresa, Italy, 2006.
- [45] S. P. Beeby, R. N. Torah, M. J. Tudor, P. Glynn-Jones, T. O'Donnell, C. R. Saha, and S. Roy, "A micro electromagnetic generator for vibration energy harvesting," *J. Micromech. Microeng.*, vol. 17, no. 7, pp. 1257–1265, Jul. 2007.
- [46] W.-S. Huang, K.-E. Tzeng, M.-C. Cheng, and R.-S. Huang, "A silicon MEMS micro power generator for wearable micro devices," *J. Chin. Inst. Eng.*, vol. 30, no. 1, pp. 133–140, Jan. 2007.
- [47] *Perpetuum PMG FSH Datasheet*, Perpetuum, Southampton, U.K., May 2010. [Online]. Available: [http://www.perpetuum.com/resources/PMG\\_FSH\\_Datasheet.pdf](http://www.perpetuum.com/resources/PMG_FSH_Datasheet.pdf)
- [48] *Ferro Solutions VE460*, F. Solutions, Woburn, MA, May 2009. [Online]. Available: [http://www.ferrosi.com/files/VEH460\\_May09.pdf](http://www.ferrosi.com/files/VEH460_May09.pdf)

- [49] I. Ayala, D. Zhu, M. Tudor, and S. Beeby, "Autonomous tunable energy harvester," in *Proc. PowerMEMS*, Washington, DC, 2009, pp. 49–52.
- [50] S. C. Chang, F. M. Yaul, A. Dominguez-Garcia, F. O'Sullivan, D. M. Otten, and J. Lang, "Harvesting energy from moth vibrations during flight," in *Proc. PowerMEMS*, Washington, DC, 2009, pp. 57–60.
- [51] E. Bouendeu, A. Greiner, P. J. Smith, and J. G. Korvink, "An efficient low cost electromagnetic vibration harvester," in *Proc. PowerMEMS*, Washington, DC, 2009, pp. 320–323.
- [52] P. Wang, X. Dai, X. Zhao, and G. Ding, "A micro electromagnetic vibration energy harvester with sandwiched structure and air channel for high energy conversion," in *Proc. PowerMEMS*, Washington, DC, 2009, pp. 296–299.
- [53] R. Tashiro, N. Kabei, K. Katayama, E. Tsuboi, and K. Tsuchiya, "Development of an electrostatic generator for a cardiac pacemaker that harnesses the ventricular wall motion," *J. Artif. Organs*, vol. 5, no. 4, pp. 0239–0245, Dec. 2002.
- [54] G. Despesse, J. J. Chaillout, I. Dekkaki, T. Jager, J. M. Leger, A. Vassilev, S. Basrou, and B. Charlot, "High damping electrostatic system for vibration energy scavenging," in *Proc. Nanotechnol. Conf. Trade Show*, Anaheim, CA, 2005, pp. 371–374.
- [55] D. Miki, M. Honzumi, Y. Suzuki, and N. Kasagi, "MEMS electret generator with electrostatic levitation," in *Proc. PowerMEMS*, Washington, DC, 2009, pp. 169–172.
- [56] K. Hammond, E. Lai, E. Leland, S. Mellers, D. Steingart, E. Carleton, B. Reilly, J. Baker, B. Otis, J. Rabaey, D. Culler, and P. Wright, "An integrated node for energy-scavenging, sensing, and data-transmission: Applications in medical diagnostics," in *Proc. 2nd Int. Workshop Wearable Implantable Body Sens. Netw.*, London, U.K., 2005, p. 58.
- [57] H. Tanaka, G. Ono, T. Nagano, and N. Ohkubo, "Electric power generation using piezoelectric resonator for power-free sensor node," in *Proc. IEEE Custom Integr. Circuits Conf.*, 2005, pp. 97–100.
- [58] H.-B. Fang, J.-Q. Liu, Z.-Y. Xu, L. Dong, L. Wang, D. Chen, B.-C. Cai, and Y. Liu, "Fabrication and performance of MEMS-based piezoelectric power generator for vibration energy harvesting," *Microelectron. J.*, vol. 37, no. 11, pp. 1280–1284, Nov. 2006.
- [59] T. H. Ng and W. H. Liao, "Sensitivity analysis and energy harvesting for a self-powered piezoelectric sensor," *J. Intell. Mater. Syst. Struct.*, vol. 16, no. 10, pp. 785–797, Oct. 1, 2005.
- [60] V. R. Challa, M. G. Prasad, S. Yong, and F. T. Fisher, "A vibration energy harvesting device with bidirectional resonance frequency tunability," *Smart Mater. Struct.*, vol. 17, no. 1, p. 015035, Feb. 2008.
- [61] N. M. White, P. Glynn-Jones, and S. P. Beeby, "A novel thick-film piezoelectric micro-generator," *Smart Mater. Struct.*, vol. 10, no. 4, pp. 850–852, Aug. 2001.
- [62] W. Lei and F. G. Yuan, "Vibration energy harvesting by magnetostrictive material," *Smart Mater. Struct.*, vol. 17, no. 4, p. 045009, Aug. 2008.
- [63] M. Marzencki, Y. Ammar, and S. Basrou, "Integrated power harvesting system including a MEMS generator and a power management circuit," *Sens. Actuators A, Phys.*, vol. 145/146, pp. 363–370, Jul./Aug. 2008.
- [64] D. Zhu, S. Beeby, M. Tudor, and N. R. Harris, "A self powered tag for wireless structure health monitoring in aeronautical applications," in *Proc. PowerMEMS*, Washington, DC, 2009, pp. 201–204.
- [65] R. Elfrink, M. Renaud, T. M. Kamel, C. de Nooijer, M. Jambunathan, M. Goedbloed, D. Hohfeld, S. Matova, and R. van Schaijk, "Vacuum packaged MEMS piezoelectric vibration energy harvesters," in *Proc. PowerMEMS*, Washington, DC, 2009, pp. 67–70.
- [66] R. Elfrink, T. M. Kamel, M. Goedbloed, S. Matova, D. Hohfeld, Y. van Andel, and R. van Schaijk, "Vibration energy harvesting with aluminum nitride-based piezoelectric devices," *J. Micromech. Microeng.*, vol. 19, no. 9, p. 094005, Sep. 2009.
- [67] D. Berdy, P. Srisungsithisunti, X. Xu, J. Rhoads, B. Jung, and D. Peroulis, "Compact low frequency meandered piezoelectric energy harvester," in *Proc. PowerMEMS*, Washington, DC, 2009, pp. 71–74.
- [68] J. C. Park, D. H. Lee, J. Y. Park, Y. S. Chang, and Y. P. Lee, "High performance piezoelectric MEMS energy harvester based on D33 mode of PZT thin film on buffer-layer with PBTIO3 inter-layer," in *Proc. Int. Solid-State Sens., Actuators, Microsyst. Conf., TRANSDUCERS*, 2009, pp. 517–520.
- [69] M. Khbeis, J. McGee, and R. Ghodssi, "Development of a simplified hybrid ambient low frequency, low intensity vibration energy scavenger system," in *Proc. Int. Solid-State Sens., Actuators, Microsyst. Conf., TRANSDUCERS*, 2009, pp. 525–528.
- [70] M. Renaud, P. Fiorini, R. van Schaijk, and C. van Hoof, "An impact based piezoelectric harvester adapted to low frequency environmental vibrations," in *Proc. Int. Solid-State Sens., Actuators, Microsyst. Conf., TRANSDUCERS*, 2009, pp. 2094–2097.
- [71] W. T. Thomson, *Theory of Vibration With Applications*. Englewood Cliffs, NJ: Prentice-Hall, 1988.



**Tzeno Galchev** (M'11) received the B.S. degree in both electrical and computer engineering and the M.S. and Ph.D. degrees in electrical engineering from the University of Michigan, Ann Arbor, in 2004, 2006, and 2010, respectively.

He is currently a Research Fellow in the Department of Electrical and Computer Engineering and the Engineering Research Center for Wireless Integrated MicroSystems (WIMS), University of Michigan. His research interests lie in the development of autonomous microsystems including the development

of energy harvesting devices, sensors, actuators, analog and digital integrated circuits, and microfabrication and packaging technologies.

Dr. Galchev was the sole recipient of the University of Michigan Excellence in Engineering Fellowship in 2006, the support for which was provided by Sandia National Laboratories, Albuquerque, NM. In 2008, he was nominated for the John Atanasoff Award and was one of two finalists awarded by the President of Bulgaria for their contributions to the information society. The John Atanasoff Award is given to young scientists under the age of 36 for significant contributions in the development of information technologies.



**Hanseup Kim** (S'00–M'06) received the B.S. degree in electrical engineering from the Department of Electrical Engineering, Seoul National University, Seoul, Korea, in 1997, and the M.S. and Ph.D. degrees in electrical engineering from the Department of Electrical Engineering and Computer Science, University of Michigan, Ann Arbor, in 2003 and 2006, respectively.

From 2006 to 2009, he held a Postdoctoral Research Fellow position at the Engineering Research Center for Wireless Integrated MicroSystems

(WIMS), University of Michigan. Since 2009, he has been a USTAR Assistant Professor in the Department of Electrical and Computer Engineering, The University of Utah, Salt Lake City. His research interests include the design, fabrication, and testing of MEMS actuators and sensors; technologies and structures for polymer-based bioapplications; micro energy harvesting devices; analog and digital integrated circuits for MEMS; and micropackaging technologies.

Dr. Kim was a recipient of both the Best Paper Award and the 1st Place Award in the Design Automation Conference Student Design Contest in 2001 with four other coauthors. He was also a recipient of the Best Paper Award at the International Conference on Commercialization of Micro and Nano Systems (COMS 2008) with eight other coauthors.



**Khalil Najafi** (F'00) received the B.S., M.S., and Ph.D. degrees in electrical engineering from the University of Michigan, Ann Arbor, in 1980, 1981, and 1986, respectively.

He has been the Schlumberger Professor of Engineering and the Chair of Electrical and Computer Engineering, University of Michigan, since September 2008. He served as the Director of the Solid-State Electronics Laboratory from 1998 to 2005. He has also been the Director of the National Science Foundation's National Nanotechnology Infrastructure Network since 2004 and the Deputy Director of the NSF Engineering Research Center for Wireless Integrated MicroSystems (WIMS), University of Michigan. His research interests include micromachining technologies, micromachined sensors, actuators, and MEMS; analog integrated circuits; implantable biomedical microsystems; micropackaging; and low-power wireless sensing/actuating systems. He has been active in the field of solid-state sensors and actuators for 30 years. He has served as Associate Editor or Editor for several journals.

Dr. Najafi has been involved in several conferences and workshops dealing with microsensors, actuators, and microsystems, including the International Conference on Solid-State Sensors and Actuators, the Hilton-Head Solid-State Sensors and Actuators Workshop, and the IEEE/ASME Micro Electromechanical Systems (MEMS) Conference. He is a Fellow of the American Institute for Medical and Biological Engineering (AIBME).

Dr. Najafi has been involved in several conferences and workshops dealing with microsensors, actuators, and microsystems, including the International Conference on Solid-State Sensors and Actuators, the Hilton-Head Solid-State Sensors and Actuators Workshop, and the IEEE/ASME Micro Electromechanical Systems (MEMS) Conference. He is a Fellow of the American Institute for Medical and Biological Engineering (AIBME).